Chrysoula Bliatsiou[1],*
Jörn Villwock[1]
Daniel Topalovic[2]
Robert Pascal Panckow[3]
Steffi Knorn[2]
Matthias Kraume[1]

Characterization of the Dynamic Behavior of a Stirred Liquid–Liquid System for Process Control

The dynamic behavior of a toluene/NaOH solution system was studied in a batch stirred tank. Characterization by step response experiments showed that the drop size response to stirrer speed steps behaves as a first-order system, whereas the stirrer speed responds as a second-order system. The respective time constants differed by at least one order of magnitude, suggesting effective control of the drop size is feasible by adjusting the stirrer speed. Based on experimental data, simple, linear system models were derived for the mean drop diameter and the interfacial area using the stirrer speed as input variable. Validation experiments showed good model qualities of about 70 % and the design of test trajectories proved the model's usability in an open-loop control.

Supporting Information available online

Keywords: Drop size distribution, Liquid–liquid system, Process control, Stirred tank reactor

Received: August 19, 2024; *revised:* November 19, 2024; *accepted:* December 23, 2024

DOI: 10.1002/ceat.202400371

1 Introduction

1.1 State of the Art

Continuous mixer-settler systems are widely applied in liquid–liquid extraction processes. The two unit operations have different tasks and require opposing conditions with respect to drop sizes that make it challenging to operate the total process. Although tiny droplets with a large specific interfacial area are preferable for the mass transfer in the extraction step inside the stirred vessel, larger drops are beneficial for the following settling step in the separator. The drop size distribution (DSD) is determined by the applied stirrer speed and the corresponding power input in the stirred tank.

Even when industrial apparatuses are equipped with stirrer speed control, the speed is typically maintained at a constant value, primarily based on practical experience rather than on closed-loop feedback control. Only biogas reactors sometimes work with intermittent stirring as it can either enhance the biogas production or save a significant amount of energy with constant biogas production compared to continuous stirring [1]. However, even here, the stirring intervals are set based on practical knowledge and adjusted through trial-and-error methods rather than by systematic feedback control. Usually, operation parameters might only be changed if the overall process efficiency is affected, e.g., when concentrations of by-products exceed a certain limit or if the product yield is too low. It is somewhat surprising that the flexibility to operate the stirred tank by controlling the stirrer speed over a wide range is seldom exploited. One reason for that might often be missing in situ measurements and, in the case of drop sizes, the lack of real-time data that is crucial for process control.

Even in academic research, the benefits of speed control are rarely used and closely investigated. The application of unsteady mixing instead of standard mixing was recommended by different authors for the laminar single-phase mixing of high viscous fluids [2–4]. They observed enhanced mixing efficiency using unsteady stirring conditions (e.g., ramps, step, or sinusoidal functions) and explained the more homogeneous mixing with the creation of chaotic flow that reduces segregated regions, so called isolated mixing regions.

Some scientific effort was put on batch and fed-batch aerobic fermentations in bioreactors with controlled stirrer speed. Besides dissolved oxygen (DO) as one significant parameter in the cultivation process, also the shear sensitivity of microorganisms must be considered. Although DO concentrations can be measured online and in real time, the DO control is challenging due to the process dynamics and the complex nonlinear behavior. Some groups developed DO control strategies by adapting the stirrer speed and either aeration rate or temperature [5–8]. But in general, tuning difficulties were reported when conventional PI controllers with fixed parameters were used for DO control. A control strategy based on PID control and gain scheduling of the stirrer speed was suggested to account for the process

---

[1] M.Sc. Chrysoula Bliatsiou https://orcid.org/0000-0001-9394-0031 (c.bliatsiou@tu-berlin.de), Dr.-Ing. Jörn Villwock https://orcid.org/0000-0002-2958-0817, Prof. Dr.-Ing. Matthias Kraume https://orcid.org/0000-0002-3116-7220
Technische Universität Berlin, Chair of Chemical and Process Engineering, ACK 7, Ackerstr. 76, 13355 Berlin, Germany.
[2] M.Sc. Daniel Topalovic https://orcid.org/0009-0004-8349-0099, Prof. Dr. Steffi Knorn https://orcid.org/0000-0002-4413-4225
Technische Universität Berlin, Chair of Control, ER 2-1, Hardenbergstr. 63a, 10623 Berlin, Germany.
[3] M.Sc. Robert Pascal Panckow
SOPAT GmbH, Bergholzstr. 8, 12099 Berlin, Germany.

variations [9]. Furthermore, more advanced DO control approaches like a Model Reference Adaptive Control scheme using the stirrer speed as a control signal were presented [10].

In liquid–liquid systems, the variation of stirrer speed for process control has been less frequently documented. For instance, in the suspension polymerization of styrene, it was reported that particle size could be changed widely with a high degree of uniformity by changing the stirrer speed using a double impeller [11] or employing the co-reverse rotational method with a periodic time interval [12]. In contrast, in batch precipitation of silica in stirred tanks, particle size distributions (PSDs) produced were found to be independent of stirrer speed mode—whether fixed or variable. This suggests that energy consumption can be reduced without compromising product quality [13]. However, for liquid–liquid dispersions, the proposed use of a linear quadratic regulator (LQR) based on simulations using population balance equations (PBEs) indicated that further analysis of the problem, i.e., the model identification, is necessary as no influence of the LQR on the DSDs in simulations could be found [14].

Despite existing technical capabilities for controlling stirrer speeds in industrial applications, no examples are published. This does not necessarily mean that such concepts are not used at all, but it does suggest that such approaches are not yet considered standard practice. In some industrial scenarios, such as batch or fed-batch processes, the stirrer speed is varied, particularly in polymerizations where the stirrer speed must be reduced due to the increasing viscosity as the reaction progresses. Similarly, in some industrial batch extraction processes, the stirrer speed is reduced at the end of the mass transfer process before the stirrer is completely switched off to reduce the time for the following settling process. These adjustments are typically based on empirical experience rather than on systematic control.

Because there are great improvements in the computational handling of big data (e.g., ML methods) and the progress in real-time acquisition of process parameters such as drop sizes, the potential of adaptive stirring speed by closed-loop control can also be used in continuous industrial processes soon. An illustrative example for such a closed-loop control was demonstrated for a small lab-scale stirred DN32 liquid–liquid extraction column [15]. The authors implemented a control strategy for the fluid dynamics based on convolutional neural networks (CNNs). Optical drop size determination via the CNN was used as input for feedback control to adjust the stirrer speed and volume flow rate, aiming for stable operation conditions. Only three classes of drop sizes (small, medium, and large) were determined, rather than a complete DSD. However, the comprehensive understanding of the DSD, combined with concentration measurements, is crucial for accurately assessing and controlling the mass transfer performance.

This research project focuses on a liquid–liquid mixer-settler system, with the goal of optimizing the process via closed-loop control of drop sizes using the stirrer speed as the feedback input. The primary challenge is to establish optimal stirrer speed control trajectories that balance effective mass transfer—facilitated by smaller drops and a larger interfacial area—and efficient phase separation in the settler, where larger drops expedite settling time. To address this, the development of control trajectories must be based on a process model that can accurately describe the dynamic system behavior.

To build such a process model, only the mixer unit, i.e., a stirred tank reactor (STR) in batch operation, is considered in the process chain at the initial stage of investigation. In this article, the dynamic behavior of a selected liquid–liquid system (here without mass transfer) in the batch STR is investigated. Stirring experiments are conducted to determine the DSDs of the material system under varying stirrer speeds and step functions. These experimental results, along with standard test signals, are utilized to identify and validate a dynamic model of the DSD where the stirrer speed acts as a key input variable. As a result, the validated model is used to design test control trajectories for the current open-loop process control.

Optimization of the overall process requires a closed-loop control. Therefore, the integration of a real-time DSD determination using neural network particle detection is currently in progress. Once the closed-loop control is established, the STR will be operated in continuous mode, and at a later stage, the settler unit will also be added to the process chain to study and optimize the complete system operation.

1.2 Description of Liquid–Liquid Dispersions

The Sauter mean diameter d_{32} is the most commonly used parameter for describing the DSD in liquid–liquid systems. It represents the diameter of a drop whose volume/surface area ratio equals the mean volume/surface area ratio of the distribution and is directly related to the dispersed phase fraction φ_d and the total interfacial area per total volume a in the system $d_{32} = 6\varphi_\mathrm{d}/a$.

Additionally, the Weber number (We), which is a dimensionless number relating the kinetic energy of a droplet to its surface energy, often correlates with d_{32}. For systems with higher dispersed phase fractions $\varphi_\mathrm{d} > 5$ vol %, where both breakage and coalescence are significant, the literature typically suggests the form:

$$\frac{d_{32}}{d_{st}} = C_1\,(1 + C_2\varphi_d)\,We^{-C_3} \tag{1}$$

where C_1 depends on the stirrer type, and C_2 quantifies the influence of coalescence. In the literature, the exponent of We C_3 is commonly reported to be 0.6 for breakage-dominated dispersions and 0.375 for coalescence-dominated dispersions [16]. There are several extensions and further developed We correlations available in the literature [17, 18]. Besides the accompanying huge variety of reported correlation constants, exponents, and fitting parameters, these correlations have another major limitation as they are based on the analysis of steady-state drop diameters. In steady state, breakage and coalescence processes are in equilibrium, and the drop size is constant over time. In most industrial applications, such as solvent extraction, polymerization, and biocatalytic processes, transient DSDs occur that cannot be described by such correlations.

For describing the time evolution of a DSD, the PBE is predominantly applied. This modular framework separates the processes of drop breakage and coalescence in a drop swarm, describing changes in the number density function $f(d_p,t)$, which represents the distribution of drops with diameter d_p within a certain volume over time. The PBE incorporates birth and death terms for each drop based on submodels that handle breakage and coalescence events independently. A wide range of modeling approaches for these submodels with different levels of detail is available in the literature. There are extensive reviews of submodels for drop breakage [19–22], drop coalescence [21, 23–25], and also approaches for gravity settlers [26, 27]. The principal advantage of using PBE is the possibility to calculate not only the complete DSD and the corresponding moments of the distribution in steady state but, more important also under transient conditions. However, due to the vast array of submodels, each designed to incorporate a large number of influencing factors, it is difficult to select the appropriate model for a specific problem or material system [28]. The complexity required for accuracy must be balanced against the solvability of the models to ensure computational efficiency. Especially in the case of coalescence, developed submodels are based on diverse assumptions and simplifications that result in different and partly contradictory dependencies on influencing factors [29]. Moreover, a vast variety of fit parameters for the implemented submodels is available, and the determination of these interdependent fit parameters is crucial for the performance and accuracy of the simulations [30].

Unfortunately, most models for the description of DSD suffer from significant shortcomings when it comes to using them for control. Specifically, models based on *We* lead only to static instead of dynamic equations, whereas models based on PBEs usually contain a great number of parameters, making experimental identification challenging. To circumvent such difficult to parameterize models, linear models of higher degree for interfacial area, based on calculations using the Sauter mean diameter and the average droplet size directly from the experimentally measured distributions, are identified. For this purpose, a data-driven black-box approach using AutoRegressive with eXogenous input (ARX) models was chosen. This approach offers the advantage of being easier to parameterize and quicker to perform, using established methods and implementations via Matlab. Although an error-free model description cannot be expected from such an approach, it is still anticipated that characteristic system behavior can be sufficiently well described by such a model. This should allow for qualitative improvements in system behavior through dynamical open-loop control based on such a model, in contrast to classic static open-loop control [31].

2 Materials and Methods

2.1 Material System

In this study, the investigated liquid–liquid system consisted of toluene (1.08325.6025, Merck KGaA) as dispersed phase and an aqueous NaOH solution with a concentration of $c_c = 0.1\ \text{mol L}^{-1}$ (1.09956.0001, Merck KGaA) as continuous phase. The volume phase fraction of the dispersed phase was set at $\varphi_d = 10$ vol %. Toluene has a density of $\rho_d = 870\ \text{kg m}^{-3}$ and a dynamic viscosity of $\eta_d = 0.54$ mPa s, whereas the continuous phase has $\rho_c = 1000\ \text{kg m}^{-3}$ and $\eta_c = 0.89$ mPa s, with all properties measured at 20 °C. Due to CO_2 absorption, the pH of the continuous phase, which was always determined at the beginning of each experiment, was found to be $pH = 12.69 \pm 0.2$. The interfacial tension between the phases was experimentally determined to be $\gamma = 28\ \text{mN m}^{-1}$ at 20 °C.

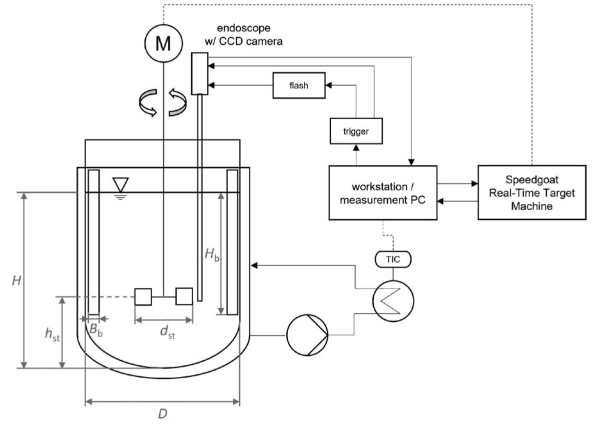

Figure 1. Schematic flow sheet of the experimental setup.

2.2 Experimental Setup

The experiments were carried out in a double-walled glass reactor with a hemispherical bottom. The inner diameter was $D = 150$ mm, and a chosen filling height $H/D = 1$. An overhead stirrer (Eurostar 60 control, IKA GmbH) capable of speeds up to 2000 min^{-1} was employed. A radial-flow Rushton turbine, with a diameter of $d_{st} = 50$ mm, served as agitator ($Ne_{turb} = 3.8$). The stirrer off-bottom clearance, defined as the distance between the centerline of the turbine disk and the tank bottom, was set at $h_{st} = 0.33\ D$. Four equally spaced stainless-steel baffles with a width $B_b = 10$ mm and immersed length $H_b = 102$ mm prevented vortex formation, thereby enhancing secondary flow and improving the overall mixing efficiency. The system temperature was maintained at a constant 20 °C, controlled via an external thermostat. A schematic flow sheet of the setup is depicted in Fig. 1.

The control of the stirrer speed was managed using a baseline real-time target machine, the Speedgoat Type Baseline S (Speedgoat GmbH). The connection between Speedgoat and stirrer was established via serial communication, utilizing the respective ports of both machines. This setup allowed for a minimal sample time of 0.1 s, ensuring error-free communication. The control program used to trigger the stirrer was initialized via Matlab, built in Simulink, and finally loaded onto the Speedgoat using the Simulink Real-Time workflow.

For the batch experiments, the range of stirrer speeds investigated was $N = 450\text{–}700\ \text{min}^{-1}$, which corresponded to a range of mean energy dissipation rate $\varepsilon = 0.25\text{–}0.94\ \text{W kg}^{-1}$ and Reynolds numbers of $Re = 17\,711\text{–}27\,550$. The minimum stirrer speed $N_{min} = 450\ \text{min}^{-1}$ was selected to ensure fully developed dispersion, whereas the maximum speed $N_{max} = 700\ \text{min}^{-1}$ was set to prevent surface aeration.

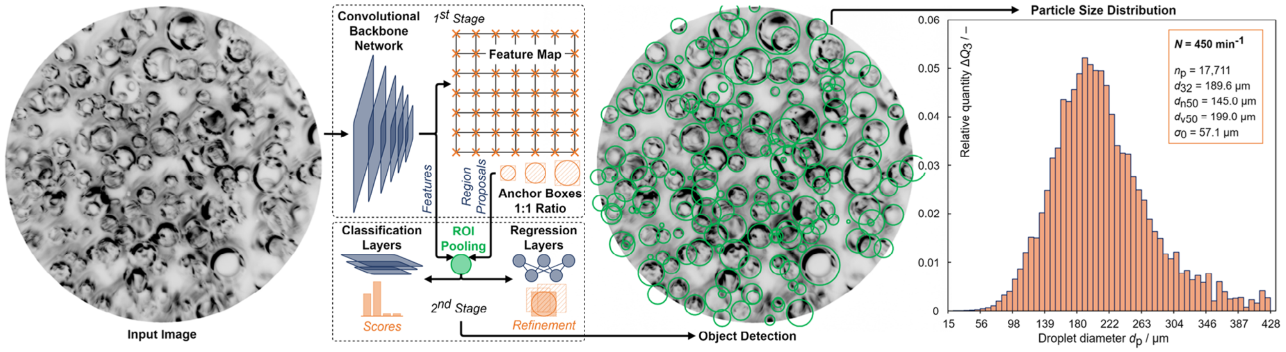

Figure 2. Signal processing chain from raw data acquisition to result output, utilizing a modified Faster R-CNN as core component for object detection. For better visual recognition, the endoscope images presented in the figure have been inverted.

2.3 Particle Measurement Technique

The DSDs were measured using a photo-optical endoscopic measurement technique (SOPAT GmbH). The employed probe type SOPAT Sc features a field of view of 2.7 mm and can reliably capture particles in the size range of $d_p = 9$–1200 µm. Endoscopically obtained in situ images serve as the two-dimensional (2D) raw data input for the signal processing chain toward final measurement values, as graphically depicted in Fig. 2.

Images are acquired at 20 Hz with a resolution of 2476 × 1980 pixel per single image (90 % ROI of full sensor). A series of 20–100 images is acquired and is, without further pre-processing, jointly batch-processed to define each single data point. A sufficient number of detected particles ranging from 2000 to 4000 per image series was detected to ensure statistically stable data points.

Image analysis is carried out offline in batches of image series, i.e., data points. The core component of the particle analysis is a CNN, which outputs 2D recognized and measured objects. The ensemble of all particle detections across all images in a series is used to define the particle distribution for that data point. The distributions are then used to derive the characteristic values such as d_{10}, σ_0, and d_{32}.

The employed CNN is a custom variant of Faster R-CNN [32, 33], modified by SOPAT to detect spherical particles [34]. This modification allows for an end-to-end setting (raw image in, segmented instances out). To train the CNN, the stochastic gradient descent optimizer was chosen. The training data consisted of 22 individual subsets, totaling 139 manually annotated images. This includes in total 25 462 marked particles (particles per image: min. 36, max. 877, avg. 183.18). All training data were endoscopically acquired from systems containing solely spherical droplets. The various subsets define different material systems (all liquid–liquid) under completely different operating conditions.

2.4 Modeling

Here, a brief overview of the derived system model is given. For a detailed description, please refer to [31]. This work initially investigates a binary liquid–liquid system without mass transfer. For the explicit modeling of the dynamic system describing the coalescence and breakage of the droplets in the stirred tank, two key characteristics to describe the system behavior were used, both of which are directly derived from the SOPAT image analysis data described in Sect. 2.5. The operational quality regarding mass transfer is assessed based on the interfacial area of droplets a, calculated via the measured DSD. An increase in interfacial area is beneficial for the mass transfer and, thus, maximizing the interfacial area during the experiment in the stirred tank defines desired operation conditions. For the phase separation occurring in a downstream settler, larger droplet sizes are preferable; therefore, assuming a batch-like operation here, larger droplet sizes at the end of the experiment are targeted. These droplet sizes are characterized using the mean droplet diameter d_{10}, calculated from the experimental distributions.

Given the droplet diameters $d_i(t)$ at a discrete time instant t from a distribution with n_D data points, the diameter $d_{10}(t)$ can be calculated as follows:

$$d_{10}\left(t\right) = \frac{1}{n_D}\sum_{i=1}^{n_D} d_i\left(t\right) \tag{2}$$

To enhance the robustness of the signal describing the interfacial area $a(t)$, it is calculated based on a reformulation of the definition of the Sauter mean diameter d_{32} as follows:

$$a\left(t\right) = \frac{6V}{d_{32}\left(t\right)} \tag{3}$$

Eq. (3) utilizes the Sauter mean diameter, calculated via SOPAT, and the constant toluene volume of $V = 200$ mL, which is $\varphi_d = 10$ vol %.

Both $d_{10}(t)$ and $a(t)$ are modeled as functions of the effective stirrer speed $N(t)$ using ARX models. For a given input $u(t)$ (here the stirrer speed $N(t)$) and output $y(t)$ (here either the mean drop size $d_{10}(t)$ or the total drop interfacial area $a(t)$, respectively), the relation between actual and past values is expressed as follows:

$$\begin{aligned} &y\left(t\right) + a_1 y\left(t-1\right) + \cdots + a_{n_a} y\left(t-n_a\right) \\ &\quad = b_1 u\left(t-n_k\right) + \cdots + b_{n_b} u\left(t-n_b-n_k+1\right) + e\left(t\right) \end{aligned} \tag{4}$$

The parameters n_a and n_b are the orders of the ARX model, and n_k is the delay. $e(t)$ is a noise signal that contains normally distributed noise, which is defined internally in Matlab to improve the model performance.

By introducing the shift operator q, Eq. (4) can be reduced to

$$A\left(q\right) y\left(t\right) = B\left(q\right) u\left(t-n_k\right) + e\left(t\right) \tag{5}$$

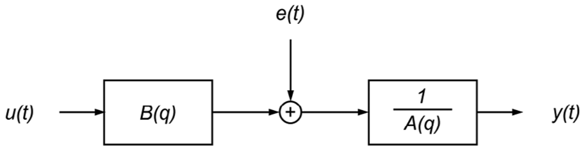

Figure 3. Block diagram of the used AutoRegressive with eXogenous input (ARX) model.

with

$$A(q) = 1 + a_1 q^{-1} + \cdots + a_{n_a} q^{-n_a} \tag{6}$$

$$B(q) = b_1 + b_2 q^{-1} + \cdots + b_{n_b} q^{-n_{b+1}} \tag{7}$$

The generic block diagram for the ARX model is shown in Fig. 3. The detailed polynomial equations $A(q)$ and $B(q)$ for $d_{10}(t)$ and $a(t)$, respectively, can be found in the Supporting Information section.

2.5 Experiments

In the present study, two types of experiments, i.e., step functions and identification experiments, were conducted to derive the dynamic model.

The initial experimental part aimed to characterize a relatively slowly coalescing liquid–liquid system suitable for process control. This phase involved extensive studies on the system's coalescence and breakage behaviors, time constants, reproducibility, range of drop sizes, and the self-similarity of DSDs. During this phase, step functions were applied during mixing. In particular, the dispersion was stirred at a constant stirrer speed until a steady state was reached. The stirrer speed was then abruptly—either increased or decreased—to induce drop breakage or coalescence, respectively. The step response of DSDs was observed and measured using the endoscope. As the stirrer speed changed stepwise, the transient development of the DSDs was closely monitored, with image series acquisition taking place every 2–4 s until a new steady state was reached. Once the steady state was attained, where the distributions remained practically unaltered, the frequency of endoscope image acquisition was reduced to up to one image series every 2.5 min.

In the second experimental phase, experiments were performed to excite the higher frequency range of the system, which is crucial for the identification of higher order dynamic models. Two types of input signals were employed: chirp and pseudo random binary sequence (PRBS), each serving distinct purposes. The chirp, which was used for the auto-validation, meaning the actual fitting of model parameters, was a sinus signal lasting 1190 s. It swept through a frequency range of $f = 10^{-4}$–1.66×10^{-2} Hz with an amplitude of 125 min^{-1}. Conversely, the PRBS was used for cross-validation of the model. Defined as a 3600 s long signal with a sample time of 0.1 s and a minimum holding time of 10 s for each stirrer speed step. Figures of the two used signals can be found in the Supporting Information section. Based on the obtained models, an optimization problem was formulated that allowed the calculation of two dynamically changing stirrer speed trajectories to serve as a proof of concept (see Eq. 8):

$$\underbrace{\begin{bmatrix} y(0) \\ y(1) \\ y(2) \\ \dots \\ y(K) \end{bmatrix}}_{\underline{Y}} = \underbrace{\begin{bmatrix} \mathbf{D} & 0 & 0 & \dots & 0 \\ \mathbf{CB} & \mathbf{D} & 0 & \dots & 0 \\ \mathbf{CAB} & \mathbf{CB} & \mathbf{D} & \dots & 0 \\ \dots & \dots & \dots & \dots & \dots \\ \mathbf{CA}^K\mathbf{B} & \mathbf{CA}^{K-1}\mathbf{B} & \mathbf{CA}^{K-2}\mathbf{B} & \dots & \mathbf{D} \end{bmatrix}}_{G_y} \underbrace{\begin{bmatrix} u(0) \\ u(1) \\ u(2) \\ \dots \\ u(K) \end{bmatrix}}_{\underline{U}} \tag{8}$$

To do this, the identified ARX models are transformed into their respective state-space representations (matrices $\mathbf{A}, \mathbf{B}, \mathbf{C}, \mathbf{D}$). Using these matrices and the fact that the system is linearly described, the system responses $\underline{Y}_i$ in mean drop size (index m) and surface area (index a) to an actuation $\underline{U}$ over a period of length K were described by multiplying this stacked actuation vector $\underline{U}$ by the respective stacked system matrices $\mathbf{G}_m$ and $\mathbf{G}_a$. This was used to formulate a cost function I with the respective weighting vectors $\underline{\mathbf{W}}_m$ and $\underline{\mathbf{W}}_a$ as $I(\underline{U}) = (\underline{\mathbf{W}}_m^T \mathbf{G}_m + \underline{\mathbf{W}}_a^T \mathbf{G}_a)\underline{U}$, which is minimized. Two optimizations with slightly different weights were performed using Matlab (fmincon). Only the last value of $\underline{\mathbf{W}}_m$ was non-zero (10^8), all entries of $\underline{\mathbf{W}}_a$ were the same in each optimization, and either $\mathbf{w}_a \in \{10^{13}\}$ or $\mathbf{w}_a \in \{10^{14}\}$ for trajectory 1 and 2, respectively.

3 Results

3.1 Characterization of Material System

In the initial stages of experimentation, the coalescence and breakage behavior of the selected liquid–liquid dispersion system was characterized in batch operation in the stirred tank by applying step functions during mixing. As the stirrer speed changed by an increasing or decreasing step, the transient development of the DSDs was closely monitored, until a steady state was reached. The DSD results from the two competing phenomena of drop breakage and coalescence. Although complete DSDs were measured, the use of the Sauter mean diameter as a single characteristic length of the distribution proved to be a reliable and adequate description of the system's responsiveness to changes in stirrer speed, while correlating with the total interfacial area available for mass transfer.

Fig. 4 illustrates the evolution of the Sauter mean diameter d_{32} over time t for three experiments where identical step functions were applied at the same intervals. Specifically, the stirrer speed alternated among three levels: 450, 600, and 700 min^{-1}. The stirrer speed profile is also graphically depicted. As expected, the drop sizes decrease when the stirrer speed increases (i.e., dominant drop breakage), and they increase when the stirrer speed drops (i.e., more pronounced coalescence). When the stirrer speed returns to a previous setting, both the DSD and the Sauter mean diameter revert to their prior values, demonstrating the system's consistency. A slight drift in drop diameter over time was observed in most experiments. Investigations into the origin of this drift have not linked it to variations in electrolyte composition (e.g., due to CO_2 absorption), but it could be attributed to the turbulence intermittency previously reported by other authors [35–37]. Although this drift seems to be systematic,

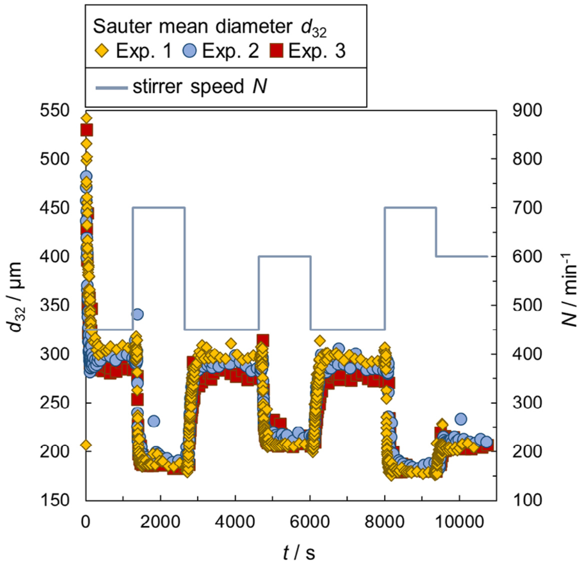

Figure 4. Development of the Sauter mean diameter over time for a given stirrer speed step profile for three experiments with the identical applied step functions.

it remains small (<4 % for the d_{32}) and in the range of typical measurement errors.

The comparison among the experimental runs confirms the good reproducibility of the system, as further corroborated by additional experimental data acquired. Deviations in the quasi steady-state Sauter mean diameter $d_{32}{}^{st}$ at the same applied stirrer speed across different runs were minimal, lying within ±(2–7) %.

All droplet size distributions determined for the specific system toluene/NaOH solution (0.1 M) exhibited Gaussian characteristics, as exemplified by the histogram shown in Fig. 2. Fig. 5a depicts the steady-state distributions for the stirrer speeds applied in Fig. 4, presented as box plots. These plots reveal a symmetric distribution around the median, confirming that the acquired distributions are normal. Moreover, these distributions demonstrated self-similarity with respect to the stirrer speed, i.e., once normalized over the respective d_{32}, they aligned along an almost identical curve, regardless of the applied stirrer speed N. This pattern is visually summarized in the probability plot of Fig. 5b for three stirrer speeds (the operation limits and an intermediate stirrer speed). Further verification was conducted for several distributions at intermediate stirrer speeds ($N = 500, 550, 650$ min^{-1}). Only minor deviations were observed at the lowest stirrer speed of $N = 450$ min^{-1}, particularly affecting the smaller droplet sizes.

To facilitate effective modeling and control design, understanding the speed at which the dispersion system responds to stirring changes is critical. Therefore, time constants characterizing this response have been determined. Fig. 6a illustrates the dynamic behavior of the system exemplarily for the largest stirrer speed steps noted in Fig. 4, specifically the step increase from 450 to 700 min^{-1} and the decrease from 700 to 450 min^{-1}. In particular, the data refer to the experimental run "Exp. 2" of Fig. 4. The determined dynamic response shown in Fig. 6a aligns with that of a first-order system, described by the step response equation:

$$d_{32}(t) = K\left(1 - e^{(-t/T_1)}\right) \tag{9}$$

where K is the gain, and T_1 the time constant. Tab. 1 presents the gains and time constants for the drop size evolution at each step of Fig. 4, averaged across runs "Exp. 1," "Exp. 2," and "Exp. 3." The shortest time constant T_1, approximately 18 s, was determined for the stirrer speed increase from 450 to 700 min^{-1}. The time constants for other steps were longer. The direction of the speed change—whether increasing or decreasing—significantly impacts the time constant. In general, drop breakage occurs much faster than drop coalescence. Accordingly, an increase in stirrer speed leads the system toward a breakage-dominant condition, accompanied by a corresponding decrease of the time constant. Conversely, with a decrease in stirrer speed,

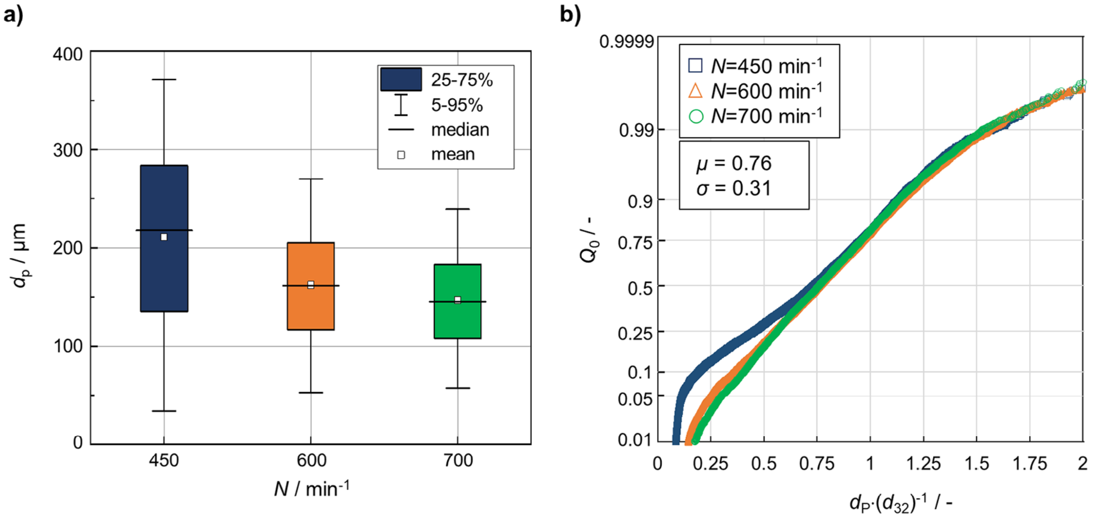

Figure 5. Steady-state distributions determined at three stirrer speeds ($N = 450, 600, 700$ min^{-1}). (a) as box plots and (b) as probability plots, the data fit to a Gaussian distribution with a mean of $\mu = 0.76$ and a standard deviation of $\sigma = 0.31$.

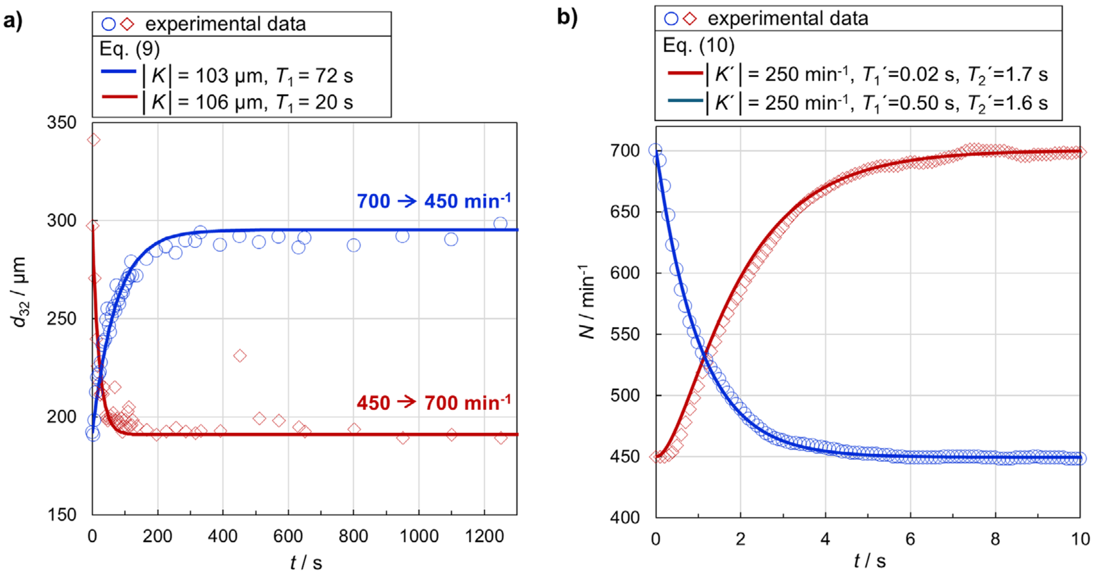

Figure 6. Dynamic responses to a step increase and decrease in stirrer speed of 250 min^{-1}, (a) of the material system, fitted with a first-order step response and (b) of the stirrer, fitted with a second-order step response to determine the time constants.

coalescence becomes the time-determining process, resulting in longer time constants.

In addition to depicting the system response, Fig. 6b shows the corresponding evolution of the stirrer speed for the step from 450 to 700 min^{-1} and back from 700 to 450 min^{-1} in Fig. 4, controlled via the Speedgoat target machine. The behavior of the stirrer can be characterized as a second-order system due to the inertia of both the stirrer and the liquid. The corresponding step response is represented by

$$N(t) = K' \left[1 - \frac{T_1{}'}{T_1{}' - T_2{}'} e^{(-t/T_1{}')} + \frac{T_2{}'}{T_2{}' - T_1{}'} e^{(-t/T_2{}')} \right] \qquad (10)$$

where K' is the gain and $T_1{}'$ and $T_2{}'$ are the time constants. As seen in Fig. 6b, the determined time constants of the stirrer are $T_1{}' < 1$ s and $T_2{}' < 2$ s. These values are notably smaller than those determined for the material system (as detailed in Fig. 6a and Tab. 1), differing by at least an order of magnitude. This significant difference in time constants between the stirrer and the material system ensures that the control of the DSD through adjustments in the stirrer speed is feasible for the specific liquid–liquid dispersion system. Experiments with a toluene/water system (at $\varphi_\text{d} = 10$ vol %) showed that the response (coalescence and breakage) to changing stirrer speed was too fast, whereas the determined time constants for the equivalent stirrer speed steps of Fig. 6a were $T_1 < 5$ s. Therefore, this system was not further used as a case study for this research work, and a relatively "slower" coalescing system was searched for, leading to the toluene/NaOH solution (0.1 M) system presented in this study.

Table 1. The determined gain K (as an absolute value) and time constant T_1 of Eq. (9) for the drop size evolution in each stirrer speed step of Fig. 4.

Stirrer speed step	Gain, $\lvert K \rvert$ [µm]	Time constant, T_1 [s]
450 min^{-1} → 700 min^{-1}	108 (±9)	18 (±2)
700 min^{-1} → 450 min^{-1}	103 (±6)	70 (±2)
450 min^{-1} → 600 min^{-1}	79 (±9)	28 (±3)
600 min^{-1} → 450 min^{-1}	77 (±9)	81 (±12)
450 min^{-1} → 700 min^{-1}	99 (±4)	17 (±3)
700 min^{-1} → 600 min^{-1}	25 (±2)	31 (±2)

Note: The system behaves as a first-order system. (In parenthesis the standard deviation among the runs).

3.2 Validation of System Model and Design of Test Trajectory

In the second experimental phase, the experiments performed aimed at identifying and validating a system model that can accurately describe the dynamic system behavior. Two types of input signals were employed: a chirp for auto-validation, which involves the actual fitting of model parameters, and a PRBS for cross-validation of the model. Detailed visualizations of both signals are provided in the Supporting Information section. This section focuses on the results of the cross-validation using the PRBS signal. For a more detailed description of the system identification and auto-validation, please refer to our previous work [31].

Fig. 7 illustrates the responses of the liquid–liquid system to the PRBS signal as deviation from the operation setpoint at $N = 575$ min^{-1} for the actual experimental data and the derived ARX model (see Sect. 2.4 and Supporting Information section). The PRBS was a 3600 s long signal with a sample time of 0.1 s and a minimum holding time of 10 s for each stirrer speed step. However, only 3350 s of this signal are depicted in Fig. 7; the remainder of the experimental period represents the time required for the system to reach a steady state at the setpoint of

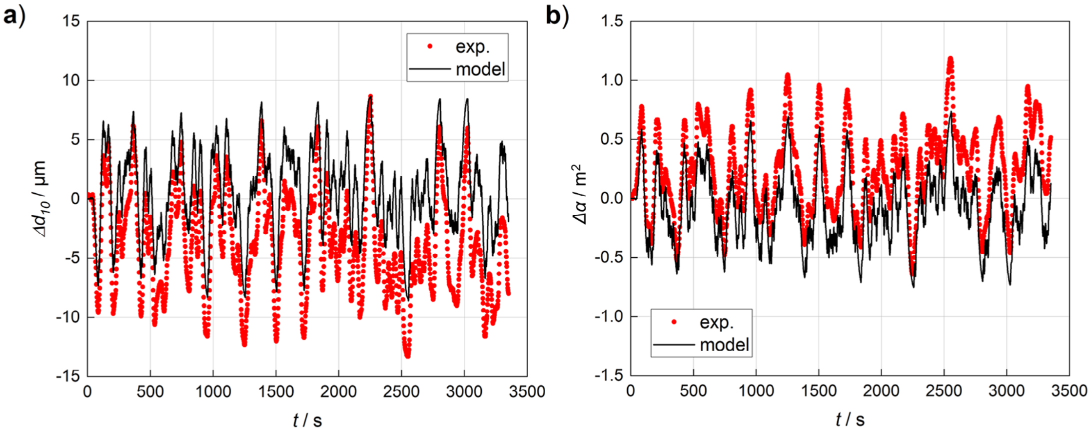

Figure 7. System response to pseudo random binary sequence (PRBS) signal; comparison of the deviation of (a) the mean droplet diameter and (b) interfacial area from operation setpoint at $N = 575\ \text{min}^{-1}$, for the experimental data and the AutoRegressive with eXogenous input (ARX) model.

$N = 575\ \text{min}^{-1}$. Fig. 7a,b illustrates the response using the metrics of the arithmetic mean drop diameter d_{10} and the total drop interfacial area a, respectively. The graphical representation provides a visual confirmation of the model's capacity to predict system behavior under varying operational conditions, highlighting its potential utility in process control.

The quality of the model in comparison to the experimental data is described herein using the normalized root mean square error:

$$\text{NRMSE} = \frac{\sqrt{\sum_{i=1}^{n} \frac{(\hat{y}_i - y_i)^2}{n}}}{y_{\max} - y_{\min}} \tag{11}$$

with n being the total number of measured values, $\hat{y}_\text{i}$ the predicted values, and y_i the measured values with $y_{\max}$ and $y_{\min}$ as the respective maximum and minimum measured values.

The model's fit quality, with a 67.9 % accuracy for the mean droplet diameter and 69.2 % for the interfacial area in this cross-validation experiment, is considered sufficiently good for a model that serves as a basis for dynamic process control applications. The maximum deviation of the model from the experimental data is up to 6 % for the mean droplet diameter and up to −8 % for the interfacial area (see Supporting Information section Fig. S3).

Overall, the model describes the process adequately well. Most notably, unlike the more complex models briefly described in Sect. 1.2, the identified model is characterized by its simplicity and linearity. Its parameters are easily identifiable through straightforward experiments that can be conducted with standard laboratory equipment. This simplicity not only makes the model more accessible but also supports the implementation of dynamic process control strategies. It allows the design of optimal control trajectories, thereby contributing to the potential optimization of the entire mixer-settler process.

Despite the overall good model fit, the deviation between experimental and model data increases with time as shown in Fig. 7 and more clearly in Supporting Information section Fig. S3 but remains in low and acceptable ranges (<10 %). The increasing deviation is attributed to the slight drift in drop sizes during stirring mentioned above. To handle the observed drift as well as variations in system behavior among different batches, a state estimation method using Extended Kalman Filter (EKF) is currently being implemented to further adapt the models identified so far. This will allow a better description and prediction of the system behavior.

As a proof of concept, the developed models were used to design two control test trajectories for the current open-loop system. Based on the theory that a large surface area is favored for mass transfer in the STR, whereas large drops are required for efficient separation in a downstream settler, two non-static trajectories were designed aiming to serve as a test of the model's applicability. The ARX models were transformed into their respective state-space representations (matrices) as described in Sect. 2.5, and a cost function was formulated to allow the optimization of both the mean drop size and surface area with slightly different weights for the two trajectories.

Fig. 8a illustrates the designed trajectories. Fig. 8b–d shows the responses of the mean droplet diameter d_{10}, the interfacial area a, and the cumulative interfacial area A_t, respectively, in direct comparison to the result for a constant stirrer speed operation (at constant minimum and maximum possible stirrer speeds for the specific setup, i.e., $N = 450$ and $700\ \text{min}^{-1}$).

The requirements for these open-loop control trajectories are simple, and therefore, their signal (Fig. 8a) appears straightforward and predictable, i.e., maximum stirrer speed was used and switched to minimum stirrer speed at the end of the experiment, at a time that varies based on the applied weights used in the cost function. Nevertheless, the results illustrate the potential of dynamic open-loop control compared to static control. The results of d_{10} and a are balanced between the two extremes of static operation, whereas the cumulative interfacial area A_t remains at its maximum throughout the experiment. Moreover, these simple test trajectories serve as an important basis for designing optimal closed-loop trajectories in future steps. More complicated requirements can be set by a corresponding configuration of the generated cost function, and in this way, different objectives can be achieved during a continuously operated process chain with a mixer and a downstream settler.

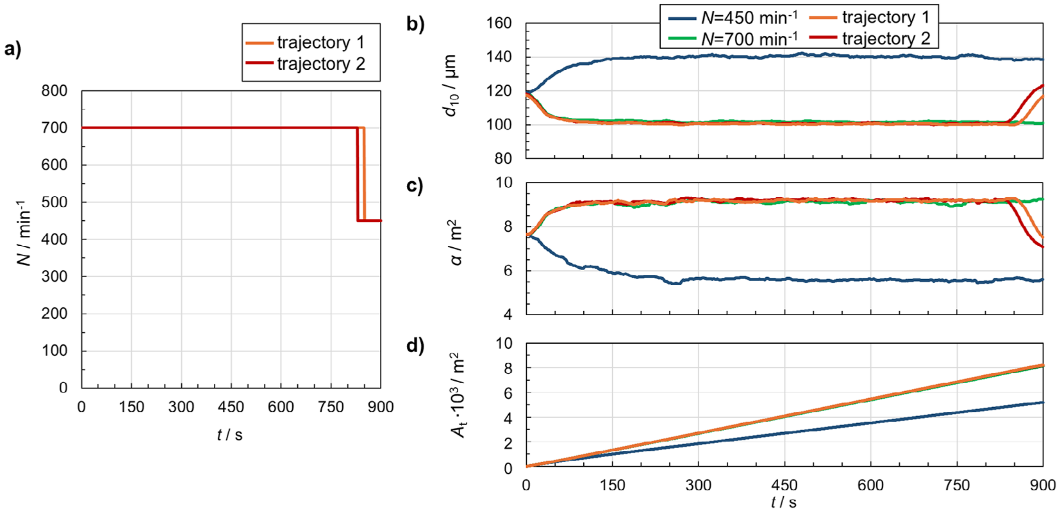

Figure 8. (a) The designed test trajectories of the stirrer speed and the responses of (b) the mean droplet diameter, (c) the interfacial area, and (d) the overall cumulative created surface area available for mass transfer throughout the experiment, in comparison to the respective outcomes of a static operation at constant minimum or maximum stirrer speed.

4 Conclusions and Outlook

The primary objective of this research is to develop a sophisticated closed-loop feedback control system that dynamically monitors and adjusts the stirrer speed based on observed DSDs in a liquid–liquid dispersion. The overall goal is to optimize a mixer-settler process, ensuring an optimal balance that maximizes mass transfer while simultaneously enhancing the separation efficiency. This goal necessitates the creation of a process model that, despite its simplicity, captures the dynamic behavior of the stirred liquid–liquid system with sufficient accuracy.

The dynamic behavior of a toluene/aqueous NaOH solution system, which serves as a case study for the investigations, was examined in a stirred tank operated in batch mode. Initial characterization of the liquid–liquid system was conducted through step response experiments, which reliably demonstrated that the drop size response to changes in stirrer speed steps was reproducible. Additionally, the development of the Gaussian DSD at steady state exhibited characteristics typical for a first-order system. Control of the stirrer was managed via a real-time target machine, which revealed that the stirrer's response adheres to a second-order control system model. The differentiation in the dynamics, with the stirrer operating on a faster time scale than the DSD changes—as indicated by the time constants differing by at least one order of magnitude—shows that dynamic control of the DSDs through the stirrer is both feasible and realistic.

Consequently, identification experiments were conducted to identify a dynamic model that describes this stirring process, wherein coalescence and breakage coexist and form the final DSDs under turbulent conditions. Validation experiments of the derived model demonstrated that, despite its simplicity as a linear function, it accurately describes the intricate dynamics of the process. The model's simplicity offers significant advantages compared to traditional static open-loop control. The applicability of the model was demonstrated by designing and applying test open-loop control trajectories.

Further research is being carried out based on the identified model. To address deviations in DSDs over time and variations in system behavior between batches, a state estimation method using EKF is currently being implemented. This will allow an even better description and prediction of the system behavior and enable the application of advanced control methods such as model predictive control.

The development and implementation of an online image acquisition system, coupled with online image analysis, is in progress. The real-time acquisition of DSD data and its integration with the stirrer control unit (Speedgoat), which manages the application of the optimum stirrer trajectories, will ultimately finally enable the establishment of a sophisticated closed-loop control system.

Finally, in a closed-loop system, the design of optimal stirrer speed control trajectories based on the identified model and its further adaptation can be carried out to optimize the complete mixer-settler system with the aim of improving mass transfer rates and separation efficiency.

This study focuses on the general methodology to develop a process model for closed-loop control. The transferability to other chemical systems and mixing equipment will be examined in future investigations.

Supporting Information

Supporting information for this article can be found under DOI: https://doi.org/10.1002/ceat.202400371.

Acknowledgments

Funded by the Deutsche Forschungsgemeinschaft (DFG, German Research Foundation)—Project number 504858152. This work is part of the DFG Priority Program SPP2364 "Autonomous processes in particle technology – Research and testing of concepts for model-based control of particulate processes".

The authors wish to thank Mr. Niclas Gasch for his experimental work, and Mr. Hsuan-Yang Shih for his assistance in the identification process.

Open access funding enabled and organized by Projekt DEAL.

Symbols used

a	[m^2]	total drop interfacial area
$a_1 \ldots a_{na}$	[–]	coefficients in Eqs. (4)–(7)
A	[–]	polynomial equations in Eqs. (5) and (6)
A_t	[m^2]	cumulative interfacial area
$b_1 \ldots b_{nb}$	[–]	coefficients in Eqs. (4)–(7)
B	[–]	polynomial equations in Eqs. (5) and (7)
B_b	[mm]	baffle width
C_1, C_2, C_3	[–]	constants in Eq. (1)
c_c	[mol L^{-1}]	base concentration of continuous phase
D	[mm]	tank diameter
d_P	[µm]	drop diameter
d_st	[mm]	stirrer diameter
d_{10}	[µm]	arithmetic mean drop diameter
d_{32}	[µm]	Sauter mean drop diameter
$e(t)$	[–]	noise signal in Eq. (4)
H	[mm]	tank filling height
H_b	[mm]	immersed baffle length
h_st	[mm]	stirrer bottom clearance
K, K'	[µm or min^{-1}]	gains in Eqs. (9) and (10)
N	[min^{-1}]	stirrer speed
Ne_turb	[–]	Newton number of stirrer in turbulent regime
n	[–]	number of measured values in Eq. (11)
n_a, n_b	[–]	model orders in Eq. (4)
n_k	[s]	delay in Eq. (4)
q	[–]	Shift operator in Eqs. (5)–(7)
Re	[–]	Reynolds number
T_1, T_1', T_2'	[s]	time constants in Eqs. (9) and (10)
t	[s]	time
$u(t)$	[min^{-1}]	input in Eq. (4)
V	[mL]	volume of the dispersed phase
y_i	[µm or m^2]	measured values in Eq. (11)
$\hat{y}_\mathrm{i}$	[µm or m^2]	predicted values in Eq. (11)
$y(t)$	[µm]	output in Eq. (4)
We	[–]	Weber number

Greek letters

ε	[W kg^{-1}]	energy dissipation rate
η	[mPa s]	dynamic viscosity
γ	[mN m^{-1}]	interfacial tension
μ	[–]	mean value
ρ	[kg m^{-3}]	density
σ	[–]	standard deviation
φ	[mL mL^{-1}]	dispersed phase fraction

Subscripts

c	continuous phase
d	dispersed phase

Superscripts

st	steady state

Abbreviations

ARX	AutoRegressive with eXogenous input
CNN	convolutional neural network
DO	dissolved oxygen
DSD	drop size distribution
LQR	linear quadratic regulator
ML	machine learning
NRMSE	normalized root mean square error
PBE	population balance equation
PI(D)	proportional-integral-(derivative)
PRBS	pseudorandom binary sequence
PSD	particle size distribution
STR	stirred tank reactor

References

[1] B. Singh, Z. Szamosi, Z. Siménfalvi, *Renew. Energy* **2019**, *141*, 922–936. DOI: https://doi.org/10.1016/j.renene.2019.04.072

[2] J.-Y. Dieulot, N. Petit, P. Rouchon, G. Delaplace, *Chem. Eng. Sci.* **2005**, *60* (*20*), 5544–5554. DOI: https://doi.org/10.1016/j.ces.2005.03.067

[3] F. Shirmohammadi, A. Tohidi, *Chem. Eng. Res. Des.* **2019**, *141*, 350–360. DOI: https://doi.org/10.1016/j.cherd.2018.04.007

[4] W. M. Yek, M. N. Noui-Mehidi, R. Parthasarathy, S. N. Bhattacharya, J. Wu, N. Ohmura, N. Nishioka, *Can. J. Chem. Eng.* **2009**, *87* (*6*), 839–846. DOI: https://doi.org/10.1002/cjce.20231

[5] K. Ogawa, C. Kuroda, H. Mizumori, S. Yoshikawa, *Kagaku Kogaku Ronbunshu* **1996**, *22* (*1*), 91–97.

[6] J. C. Rosa, A. B. Neto, C. O. Hokka, A. C. Badino, *Bioproc. Biosyst. Eng.* **2004**, *27* (*2*), 99–104. DOI: https://doi.org/10.1007/s00449-004-0386-9

[7] S. Velut, L. de Maré, P. Hagander, *Control Eng. Pract.* **2007**, *15* (*2*), 135–147. DOI: https://doi.org/10.1016/j.conengprac.2006.05.009

[8] J. Mairhofer, M. Cserjan-Puschmann, G. Striedner, K. Nöbauer, E. Razzazi-Fazeli, R. Grabherr, *J. Biotechnol.* **2010**, *146* (*3*), 130–137. DOI: https://doi.org/10.1016/j.jbiotec.2010.01.025

[9] M. Åkesson, P. Hagander, *Control of Dissolved Oxygen in Stirred Bioreactors*, *Technical Reports TFRT-7571*, Department of Automatic Control, Lund Institute of Technology (LTH) **1998**.

[10] M. Chitra, N. Pappa, A. Abraham, *IFAC-PapersOnLine* **2018**, *51* (*4*), 13–18. DOI: https://doi.org/10.1016/j.ifacol.2018.06.008

[11] M. Tanaka, T. Takahashi, I. Kimura, *Chem. Eng. Technol.* **1996**, *19* (*2*), 97–102. DOI: https://doi.org/10.1002/ceat.270190202

[12] B. Yang, K. Takahashi, *Can. J. Chem. Eng.* **2001**, *79* (*5*), 760–764. DOI: https://doi.org/10.1002/cjce.5450790509

[13] K. Quarch, M. Kind, *Chem. Ing. Tech.* **2010**, *82* (*5*), 698–703. DOI: https://doi.org/10.1002/cite.200900160

[14] J. Heiland, M. Baumann, A. Walle, V. Mehrmann, M. Schäfer, in *Proc. 4th Int. Conf. on Population Balance Model.*, September 15–17 2010, Berlin, Germany **2010**, 627–646.

[15] L. M. Neuendorf, F. Z. Baygi, P. Kolloch, N. Kockmann, *ACS Eng. Au* **2022**, *2* (*4*), 369–377. DOI: https://doi.org/10.1021/acsengineeringau.2c00014

[16] M. Kraume, A. Gäbler, K. Schulze, *Chem. Eng. Technol.* **2004**, *27* (*3*), 330–334. DOI: https://doi.org/10.1002/ceat.200402006

[17] D. E. Leng, R. V. Calabrese, *Handbook of Industrial Mixing*, Wiley, Hoboken **2003**. DOI: https://doi.org/10.1002/0471451452.ch12

[18] R. Afshar Ghotli, A. A. A. Raman, S. Ibrahim, S. Baroutian, *Chem. Eng. Commun.* **2013**, *200* (*5*), 595–627. DOI: https://doi.org/10.1080/00986445.2012.717313

[19] J. C. Lasheras, C. Eastwood, C. Martınez-Bazán, J. L. Montañés, *Int. J. Multiphas. Flow* **2002**, *28* (*2*), 247–278. DOI: https://doi.org/10.1016/s0301-9322(01)00046-5

[20] Y. Liao, D. Lucas, *Chem. Eng. Sci.* **2009**, *64* (*15*), 3389–3406. DOI: https://doi.org/10.1016/j.ces.2009.04.026

[21] N. Kopriwa, F. Buchbender, J. Ayesterán, M. Kalem, A. Pfennig, *Solvent Extr. Ion Exc.* **2012**, *30* (*7*), 683–723. DOI: https://doi.org/10.1080/07366299.2012.700598

[22] J. Solsvik, S. Tangen, H. A. Jakobsen, *Rev. Chem. Eng.* **2013**, *29* (*5*), 241–356. DOI: https://doi.org/10.1515/revce-2013-0009

[23] Y. Liao, D. Lucas, *Chem. Eng. Sci.* **2010**, *65* (*10*), 2851–2864. DOI: https://doi.org/10.1016/j.ces.2010.02.020

[24] B. Sajjadi, A. A. A. Raman, R. S. S. R. E. Shah, S. Ibrahim, *Rev. Chem. Eng.* **2013**, *29* (*3*), 131–158. DOI: https://doi.org/10.1515/revce-2012-0014

[25] J. Solsvik, H. Jakobsen, *J. Disper. Sci. Technol.* **2014**, *35* (*11*), 1626–1642. DOI: https://doi.org/10.1080/01932691.2013.866902

[26] M. C. Ruiz, R. Padilla, *Hydrometallurgy* **1996**, *42* (*2*), 281–291. DOI: https://doi.org/10.1016/0304-386x(95)00096-y

[27] B. A. Grimes, *J. Disper. Sci. Technol.* **2012**, *33* (*4*), 578–590. DOI: https://doi.org/10.1080/01932691.2011.574946

[28] L. Hohl, *Dispersion and Phase Separation in Liquid Multiphase Systems: Influence of Three Phase Conditions on Drop Size Distributions*, Ph.D. Thesis, TU Berlin **2019**. DOI: https://doi.org/10.14279/depositonce-8124

[29] J. Kamp, *Systematic Coalescence Investigations in Liquid/Liquid Systems – From Single Drops to Technical Application*, Ph.D Thesis, TU Berlin **2017**. DOI: https://doi.org/10.14279/depositonce-6528

[30] L. Hohl, S. Röhl, M. Kraume, *Chem. Eng. Technol.* **2023**, *46* (*6*), 1260–1270. DOI: https://doi.org/10.1002/ceat.202200589

[31] D. Topalovic, C. Bliatsiou, J. Villwock, M. Kraume, S. Knorn, *Online Model-Adaptation for an Unceratin Liquid-Liquid Mixer System*, in *11th Vienna International Conference on Mathematical Modelling*, February 2025.

[32] R. Girshick, *"Fast R-CNN," 2015 IEEE International Conference on Computer Vision (ICCV)*, Santiago, Chile, **2015**, pp. 1440–1448. DOI: https://doi.org/10.1109/ICCV.2015.169

[33] S. Ren, K. He, R. Girshick, J. Sun, *"Faster R-CNN: Towards Real-Time Object Detection with Region Proposal Networks,"* in *IEEE Transactions on Pattern Analysis and Machine Intelligence*, **2017**, *39* (*6*), 1137–1149. DOI: https://doi.org/10.1109/TPAMI.2016.2577031

[34] R. P. Panckow, C. McHardy, A. Rudolph, M. Muthig, J. Kostova, M. Wegener, C. Rauh, *J. Food Eng.* **2021**, *289*, 110151. DOI: https://doi.org/10.1016/j.jfoodeng.2020.110151

[35] J. Baldyga, W. Podgórska, *Can. J. Chem. Eng.* **1998**, *76*, 456–470. DOI: https://doi.org/10.1002/cjce.5450760316

[36] C. P. Peter, Y. Suzuki, J. Büchs, *Biotechnol. Bioeng.* **2006**, *93*, 1164–1176. DOI: https://doi.org/10.1002/bit.20827

[37] A. Daub, M. Böhm, S. Delueg, J. Büchs, *Chem. Eng. Sci.* **2013**, *104*, 147–155. DOI: https://doi.org/10.1016/j.ces.2013.08.023